Adsorption of hairy particles with mobile ligands: Molecular dynamics and density functional study

Cite as: J. Chem. Phys. **148**, 044705 (2018); https://doi.org/10.1063/1.5010687
Submitted: 25 October 2017 . Accepted: 11 January 2018 . Published Online: 29 January 2018

M. Borówko, S. Sokołowski, T. Staszewski, and O. Pizio

Adsorption of hairy particles with mobile ligands: Molecular dynamics and density functional study

M. Borówko,[1] S. Sokołowski,[1,a)] T. Staszewski,[1] and O. Pizio[2,b)]
[1]*Department for the Modelling of Physico-Chemical Processes, Maria Curie-Sklodowska University, Gliniana 33, Lublin, Poland*
[2]*Instituto de Investigaciones en Materiales, Universidad Nacional Autónoma de México, Circuito Exterior, 04510 Ciudad de México, Mexico*

(Received 25 October 2017; accepted 11 January 2018; published online 29 January 2018)

We study models of hairy nanoparticles in contact with a hard wall. Each particle is built of a spherical core with a number of ligands attached to it and each ligand is composed of several spherical, tangentially jointed segments. The number of segments is the same for all ligands. Particular models differ by the numbers of ligands and of segments per ligand, but the total number of segments is constant. Moreover, our model assumes that the ligands are tethered to the core in such a manner that they can "slide" over the core surface. Using molecular dynamics simulations we investigate the differences in the structure of a system close to the wall. In order to characterize the distribution of the ligands around the core, we have calculated the end-to-end distances of the ligands and the lengths and orientation of the mass dipoles. Additionally, we also employed a density functional approach to obtain the density profiles. We have found that if the number of ligands is not too high, the proposed version of the theory is capable to predict the structure of the system with a reasonable accuracy. *Published by AIP Publishing.* https://doi.org/10.1063/1.5010687

I. INTRODUCTION

The problem of description of nanoparticles at interfaces and at solid-liquid interface in particular has attracted a considerable amount of attention recently.[1–7] This interest results from scientific and technological importance of those systems.[8,9] Indeed, a better understanding of the structure and thermodynamic properties of nanoparticles at interfaces is essential for getting deeper knowledge of several important physical processes like heterogeneous catalysis, biological surface activity, biosensing, and self-assembly.[10–14]

Among different nanoparticles the so-called hybrid (or hairy) molecules that are formed from flexible chains (ligands) grafted to spherical cores play an important role.[15–18] Hairy nanoparticles combine electric, magnetic, or electronic properties of the core with flexibility and mechanical strength of the polymer brush. Numerous systems involving hairy nanoparticles have been studied. In particular, gold particles modified with different organic molecules, like surfactants, fluorinated and hydrogenated thiols, and with mixtures of organic molecules have been widely used as diagnostic or therapeutic agents and as smart nanoplatforms with maximized biospecificities, cf. the review[19] and the references quoted therein. An interesting class of hairy nanoparticles can be formed from metal cores functionalized with liquid crystals. The functionalization of metal nanoparticles with liquid crystalline polymers (e.g., with hydroxypropyl cellulose) leads to new materials exhibiting, for example, optical anisotropy.[20] The grafted liquid crystal molecules can change their spatial or orientational order under application of an external stimulus and thus they are promising candidates for future optoelectronic and metamaterial technologies.[21] Several next examples of hairy nanoparticles have been discussed in a prospective article by Fernandes *et al.*[22]

Theoretical description of systems involving hairy particles requires introduction of appropriate models. The first class of models of hairy nanoparticles assumes that the ligands are rigidly attached to the core, i.e., the positions of grafting points are fixed. The second model, however, accepts the anchor points weakly connected to the cores and, consequently, allows for their rearrangements. Such rearrangement has been observed for systems involving CdSe/CdS core-shell particles with a brush-like layer of polyethylene oxide or branched polyethyleneimine and others.[23–28] In fact, in numerous experimental systems, the anchored ligands are more or less mobile and their rearrangement on the core surface is possible.[19,21] The model with mobile ligands was used by Nikolic *et al.*[29] in their studied of self-assembly of nanoparticles modified with weakly anchored chains. Mobility of ligands can affect effective interactions between nanoparticles[30] and their self-organization.[31,32] When two particles meet together, the anchor points can slide away to make room for the cores to approach more closely. Depending on the grafting density and the length of ligands, various structures can be observed. Such effects have been reported for colloids with surface-mobile linkers.[33,34] Moreover, colloids with surface-mobile linkers play an important role in the systems of biological relevance.[35]

A great majority of theoretical studies of systems involving hybrid nanoparticles have been carried out using computer simulation methods. Besides simulations, various analytical

a)Electronic mail: stefan.sokolowski@gmail.com
b)On sabbatical leave from Instituto de Quimica de la UNAM.

approaches such as integral equation theories, density functional theories (DFTs), self-consistent field theories, and field theoretic approaches have been used. Those treatments have been outlined by Ganesan and Jayaraman.[36] However, despite the great effort, a clear understanding of the rules governing the behavior of nanoparticles at interfaces and development of theoretical tools to describe and to predict their adsorption at solid surfaces is still an open challenge.

Density Functional Theory (DFT) is a statistical-thermodynamical method to analyze structure and thermodynamic properties of several systems, including systems involving particles of a quite complex geometry[37–42] or even geometrical constructs.[43] One of the first approaches to describe adsorption of star and branched polymeric molecules was proposed by Malijevský *et al.*[44] Next, this problem was tackled in several studies.[45–48] The theories quoted above usually assume that all segments of polymers are of the same size. However, the method developed by Jiang *et al.*[49] considered polymers with different sizes of segments. Usually, successful theories of polymers combine a modified fundamental measure theory for the excluded-volume effects,[50,51] Wertheim's[52] thermodynamics perturbation theory for the polymer connectivity, and the mean field approximation for van der Waals attraction.

Formally, the architecture of hairy nanoparticles and the architecture of star polymers are quite similar. In both cases, particles are built of a central unit (core) and a number of chains (ligands) attached to it. Therefore, it is of interest to check if density functional methods developed for star polymers[44,49] could be employed to describe nonuniform systems of hairy particles.

In this work, we study the model of hairy nanoparticles with L ligands that are weakly connected to the core in contact with a hard wall. The ligands are chains and each chain is built of the same number N of identical segments. The ligands can "slide" over the core surface. We neglect the presence of a solvent. In other words, our model belongs to the class of models with an implicit solvent. According to that treatment, the presence of a continuous solvent is accounted for by introducing "effective" interactions between nanoparticles. The aim of our research is two-fold. First, using molecular dynamics simulations we compare the structure in the systems comprising of different molecules in layers adjacent to the wall. Particular systems differ by the number of ligands L and the number of segments per chain N, under the constraint of constancy of the total number of segments, $N \times L$ = constant. Our aim is also to investigate how the distribution of segments around the core changes when a particle is approaching the wall. For this purpose, we evaluate the so-called mass dipoles[53–55] and compute the histograms of their lengths and orientations with respect to the wall. The second aim of our research is to compare the results of computer simulations with theoretical predictions of a version of DFT. Of course, the information that can be gathered from DF calculations is limited in comparison with computer simulations. We concentrate in a comparison of density profiles of cores and of segments of ligands.

The paper is organized as follows. In Sec. II, we describe details of the model and of the simulations. Then, Sec. III reports the results of simulations for the systems with the total number of segments $N \times L = 36$. Section IV is divided into two subsections. First, we outline briefly the theory (Sec. IV A) and then we show representative comparisons of theory and simulations (Sec. IV B). The paper is summarized in Sec. V.

II. MODEL AND SIMULATION DETAILS

A single hairy particle is built of a spherical core of the diameter σ_0 and L ligands attached to the core. The ligands are just flexible chains and each chain comprises of N tangentially jointed spherical segments of identical diameters $\sigma_s \equiv \sigma$. We study particles with different numbers of ligands and of the segments, under the constraint of the constancy of the product $N_t = L \times N$. In other words, the total number of segments associated with a given core, N_t, is constant.

The first segment of each ligand is attached to the core at the distance $d = (\sigma_0 + \sigma)/2$. In simulations the existence of the core-grafted segment bond is assured by imposing the harmonic potential

$$u_{0s}^{(b)} = k_{0s}(r - d)^2. \tag{1}$$

Similarly, the chain connectivity is ensured by the harmonic segment-segment (ss) potentials

$$u_{ss}^{(b)} = k_{ss}(r - \sigma)^2, \tag{2}$$

acting between neighboring segments. We should stress that in theoretical calculations the model of harmonic bonds between spherical units, Eqs. (1) and (2), is replaced by the model of tangentially jointed spherical particles. This difference between models used in theory and simulations is decried in Sec. IV.

The non-bonded segment-segment (ss), segment-core ($0s$), and core-core (00) interactions are described by the Lennard-Jones (12,6) potentials

$$u_{kl}(r) = \begin{cases} 4\varepsilon_{kl}[(\sigma_{kl}/r)^{12} - (\sigma_{kl}/r)^6], & r < r_{cut,kl}, \\ 0, & \text{otherwise.} \end{cases} \tag{3}$$

In the above, $kl = ss, 0s, 00$, ε_{kl}'s are the energy parameters and $r_{cut,kl}$'s denote the cutoff distances. We use Lorentz-Berthelot combining rules for the cross interactions, $\sigma_{0s} = (\sigma_{00} + \sigma_{ss})/2$ and $\varepsilon_{0s} = \sqrt{\varepsilon_{00}\varepsilon_{ss}}$. According to our notation, $\sigma_{00} \equiv \sigma_0$, $\sigma_{ss} \equiv \sigma_s$, $\varepsilon_{00} = \varepsilon_0$, and $\varepsilon_{ss} = \varepsilon_s$. Except for the core-core interactions, the cutoff distances are $r_{cut,kl} = \sigma_{kl}$, for $kl = ss$ and $kl = 0s$, i.e., those interactions are purely repulsive. For core-core interactions, however, $r_{cut,00} = 3\sigma_0$. In our simulations, we have assumed that the entities that are directly bonded do not interact via the Lennard-Jones potential.

The particles are confined between two hard planar walls. The wall-core and the segment-core potentials are given by

$$v_0(z) = \begin{cases} 0, & \sigma_0/2 < z < L_z - \sigma_0/2, \\ \infty, & \text{otherwise} \end{cases} \tag{4}$$

and

$$v_s(z) = \begin{cases} 0, & \sigma/2 < z < L_z - \sigma/2, \\ \infty, & \text{otherwise} \end{cases}. \tag{5}$$

The Lennard-Jones diameter of segments is the unit of length, $\sigma \equiv \sigma_s$, and the core-core Lennard-Jones energy

parameter is the unit of energy, $\varepsilon \equiv \varepsilon_0$. The mass of the core molecule, m, was assumed to be the unit of mass. The mass of each segment was (arbitrary) set to $m/10$. It is obvious that dynamic properties of the system would depend on the accepted ratio of the masses. Our interest, however, is only in the evaluation of the equilibrium structure of the system.

Performing simulations we consider an ensemble of "hairy" particles in a rectangular box of the X, Y, and Z dimensions equal X_L, $Y_L = X_L$, and Z_L, respectively. The walls of the box located at $z = 0$ and $z = Z_L$ are just hard walls and the distance, Z_l, is large enough to assure the existence of the region of a uniform fluid at the middle of the box. The system is periodic in X and Y directions. The total number of segments is fixed and equal $N_t = 36$. The particles with the following pairs of the number of ligands, L, and the number of segments, N, were studied: $(L, N) = (3, 12)$, $(4, 9)$, $(6, 6)$, $(9, 4)$, and $(12, 3)$. In our study, we set $\sigma_0 = 4\sigma$ and $\varepsilon_s = \varepsilon/10$, $r_{cut,0s} = \sigma_{0s}$ and $r_{cut,ss} = \sigma$. As it has been mentioned above, the cutoff distance of the core-core Lennard-Jones (12,6) potential was $3\sigma_0 = 12\sigma$. In other words, the segments of the ligands "screen" attractive core-core forces. The energy constants of the binding potentials, k_{0s} and k_{ss}, were $1000\varepsilon/\sigma^2$. These values assure that the deviations of the bond lengths from their equilibrium values are small. The reduced length, time, and temperature are, respectively, defined as follows: $r^* = r/\sigma$, $\tau^* = \tau\sqrt{\varepsilon/(m\sigma^2)}$, and $T^* = kT/\varepsilon$. All the calculations were performed at $T^* = 2$.

Molecular dynamics simulations were carried out using LAMMPS[56,57] package. The temperature was controlled by a Berendsen thermostat. The distance Z_L ranged from 120σ to 240σ. In the majority of the runs, the box dimension X_L was 150σ, and for longer ($N \geq 9$) ligands, a bigger box was used. The total number of nanoparticles was at least 15 000 (the number of all simulated atoms was 37 times larger). Usually, the simulations were carried with $\Delta\tau = 0.002$. After equilibration (for at least 10^7 time steps), the production runs for at least 10^8 time steps were performed. The jobs were run in parallel and the number of nodes was usually 24. In order to probe uncorrelated configurations, the accumulation of the structural quantities was carried out after 100 time steps.

We evaluated local densities of cores and of segments, a pseudo-two-dimensional core-core radial distribution functions in the slabs of 1σ wide in planes parallel to the walls. We have also computed the end-to-end distances of ligands, $d_e(z)$, averaged over all ligands within a given particle in function of the distance of the core from the lower wall at $z = 0$. Moreover, for each particle, we have also calculated the mass dipole. According to the definition,[53–55] we determined the center of mass of all the segments, $\mathbf{R}_l$, first, and then the mass dipole vector is defined as $\mathbf{R}_m = \mathbf{R}_l - \mathbf{r}_0$, where $\mathbf{r}_0$ is the position of the core. The vector $\mathbf{R}_m$ characterizes the symmetry of the distribution of the segments. The orientation of the mass dipole of nanoparticles can be described as the distribution function $P(z, t)$, where $t = \cos(\theta)$ and θ is the angle between the vector $\mathbf{R}_m$ and the unit vector perpendicular to the bottom wall.

For all systems under study, we have also computed "effective" particle-wall and particle-particle interaction potentials. Definitions of these potentials and the details about their evaluation are given below.

III. SIMULATION RESULTS

The principal aim of our calculations is to determine how the structure of the nanoparticles changes with the changes of the number of ligands L and the number of segments $N = N_t/L$. Before discussing the results, we introduce codes abbreviating consecutive systems: the symbol *LiNj* denotes the system with i ligands, each composed of j segments.

Figures 1(a) and 1(b) display examples of the core local densities at high and at moderate bulk core densities, $\rho^*_{0b} = \rho_{0b}\sigma_0^3$, whereas Figs. 2(a) and 2(b) show the profiles of all segments of ligands, $\rho_s(z)$. Note that the curves from Figs. 1(a) and 2(a) have been obtained at quite high total bulk densities. If the bulk core density is ρ^*_{0b}, then the total bulk density is $\rho^*_b = \rho^*_{0b}(1 + LN\sigma^3/\sigma_0^3)$. Thus, for $\rho^*_{0b} = 0.468$ [Fig. 1(a)], the total bulk density is $\rho^*_b = 0.731$.

The first observation emerging from the presented curves is that an increase of the number of ligands (with instantaneous decrease of the number of segments per ligand) leads to increasing ordering of the cores at the wall. In fact, the curves obtained for the system $L12N3$ exhibit the existence of well-ordered layered structure extending over 5-6 layers, and even at moderate bulk density [Fig. 1(b)], this ordering is well seen. However, the profiles for the system $L3N12$ exhibit much less pronounced order, and at lower density (relevant plots have been omitted), the profile $\rho_0(z)$ possesses only a single peak in the vicinity of the wall.

Assuming that the "percentage surface coverage" of the cores can be estimated as $S = (\sigma^2/4\sigma_0^2) \times 100\%$, each grafted

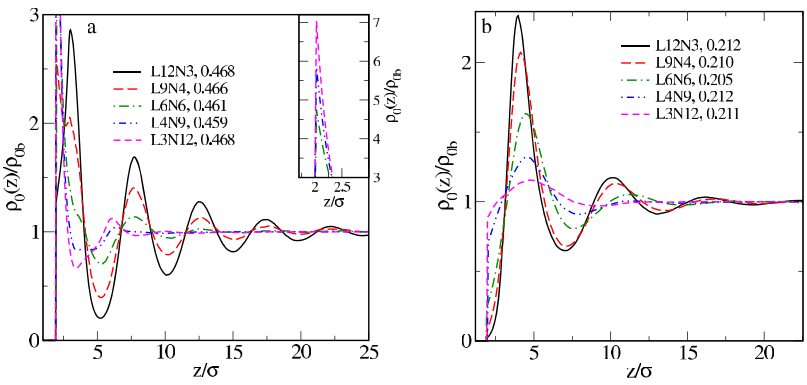

FIG. 1. Density profiles of cores, $\rho_0(z)/\rho_{0b}$, at high (a) and at moderate (b) bulk densities, $\rho^*_0 = \rho_{0b}\sigma_0^3$. The particular curves were evaluated for different values of L and N and for the values of bulk densities $\rho^*_0 = \rho_{0b}\sigma_0^3$ given in the figures. The inset of (a) shows the selected profiles at the contact with the wall, $z/\sigma = 2$.

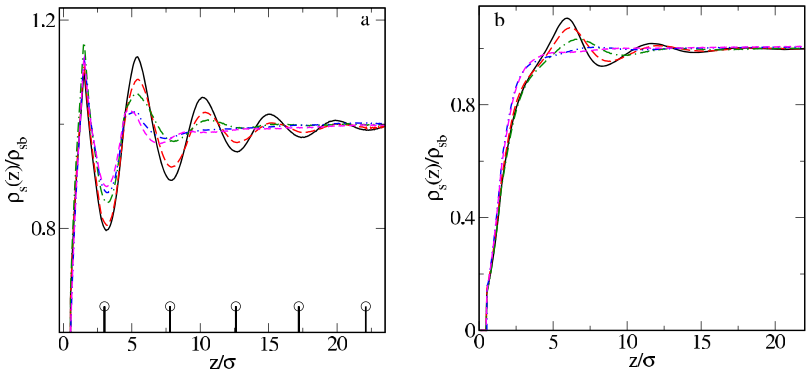

FIG. 2. Density profiles of segments, $\rho_s(z)/\rho_{sb}$. Consecutive curves in (a) [(b)] were evaluated for the same systems as the curves in Fig. 1(a) [Fig. 1(b)]. The marks on the z axis in (a) indicate the positions of the maxima of $\rho_0(z)$ for the system $L12N3$ from Fig. 1(a).

segment covers ≈1.56% of the core surface. For the largest number of ligands, $L = 12$, only 18.76% of the core surface is directly covered by the grafted segments. The segments of ligands that are not directly attached to the core also constitute obstacles in accessibility of other cores to a given core, but due to mobility, the distance of the closest approach of cores to the wall is $d_c = \sigma_0/2$ for all systems under study.

When a particle approaches the wall, the segments surrounding the core are re-arranged. The mobility of ligands increases possibility of changes of the intraparticle structure. The re-arrangement depends on the number of ligands and of course on the bulk density. If the number of ligands is smaller ($L \leq 6$), they can more easily move to the hemisphere of the core opposite to the wall and the core can "touch" the wall. This effect causes that at high bulk density the first maximum of $\rho_0(z)$ is at the distance of the closest approach, $z_{c1} = d_c$ [Fig. 1(a)]. With this respect, the system behavior resembles the behavior of a mixture of big hard spheres and smaller molecules.

For greater L (i.e., for shorter ligands), the re-arrangement is more difficult and even at high bulk density the first local density maximum moves to larger distances, $z_{c1} > d_c$. Our simulations indicated that that a decrease of the bulk density causes an increase of z_{c1}, i.e., the adsorption of the particles takes place not directly at the wall, but at a certain distance from it. This effect has been also visible for systems involving particles with long ligands.

We already know that in the case of the formation of a layered structure at a wall by Lennard-Jones molecules, the distance between consecutive local density maxima, d_m, is comparable (it is somewhat smaller) to the Lennard-Jones diameter. At high bulk densities [Fig. 1(a)], the distance between consecutive local density maxima of $\rho_0(z)$ is larger than σ_0. For the system $L12N3$, it is approximately equal to $d_m \approx 4.8\sigma$. A similar value of d_m appears for the systems $L9N4$ and $L6N6$. The situation changes for the systems $L4N9$ and $L3N12$, where d_m increases up to ≈6σ. The shape of the profiles $\rho_0(z)$ is quantitatively similar to the shape of the profiles of soft repulsive particles of diameter bigger than σ_0.

We now consider the density profiles of segments, $\rho_s(z)$; see Fig. 2. Similarly as in the case of the profiles $\rho_0(z)$, the ordering of segments is more pronounced for particles with shorter ligands. For long ligands, however, the "fluid of segments" is much less ordered and even at high bulk densities this ordering decays quickly with the distance from the wall. Of course, the ordering is more developed at higher bulk densities, while at lower bulk densities the segments just "fill" the space between the cores almost uniformly. If the segment density profiles exhibit the existence of a well-ordered structure, then the distance between consecutive local density peaks is close to the distance between the relevant peaks of the cores. Note that for the systems $L12N3$, $L9N4$, and $L6N6$ at high bulk density the consecutive minima of $\rho_s(z)$ appear at the positions of consecutive maxima of the function $\rho_0(z)$, i.e., the layers of core molecules are separated by layers composed of segments.

The distance of the closest approach of segments to the wall is $\sigma/2$. In the case of systems involving hard spheres in contact with a hard wall, the first local density maximum appears at the distance of the closest approach. However, for the systems under study, the loci of the first maxima of $\rho_s(z)$ are at larger distances z and move toward the bulk part of the system as the bulk density decreases (see Fig. 2).

At very low bulk densities, the profiles $\rho_0(z)$ resemble the profiles of particles in contact with a soft repulsive wall. Therefore, we have evaluated the "effective Boltzmann-averaged" wall-core potentials, v_{eff}. For this purpose, we simulated the density profiles $\rho_0(z)$ at two very low bulk densities ρ_{0b} and extrapolated the ratio $\rho_0(z)/\rho_{0b}$ to zero bulk density. In this manner, we evaluated the Boltzmann function, $G(z) = \lim_{\rho_{0b}\to 0}[\rho_0(z)/\rho_{0b}]$. The effective potential is defined as

$$v_{eff}(z) = -kT \ln G(z). \tag{6}$$

The plot of $v_{eff}(z)$ for the models in question is shown in Fig. 3. Note that for all models $v_{eff}(z = \sigma_0/2) = \infty$.

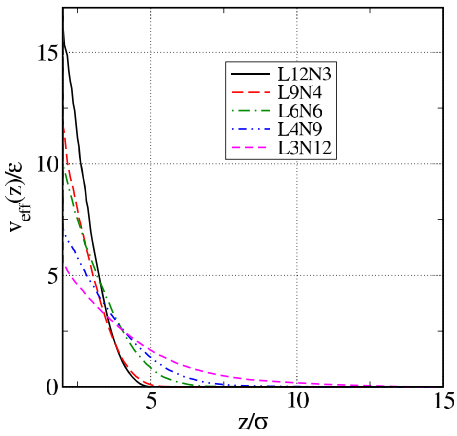

FIG. 3. Nanoparticle-wall potential of the average force for the systems with different L and N.

For the systems with longer ligands, the effective potential is less repulsive at distances close to $\sigma_0/2$ and its range is larger than for shorter ligands. This is understandable taking into account that the segments of ligands are obstacles in approaching core particles to the wall and longer ligands "act" on larger distances than shorter ones. Instantaneously, at constant total number of segments, the number of longer ligands is smaller and thus the mobility of tethered segments is easier. Note that the range of the potential $v_{eff}(z)$ is related to N by $z_{range} = \sigma_0/2 + d + (N-1)\sigma$ and at distances larger than z_{range} the potential $v_{eff}(z) = 0$.

One of the parameters that can be used to characterize the intraparticle structure is the end-to-end distance, $d_e(z)$. In our simulations, this distance was averaged over all ligands attached to a given core and presented and evaluated as a function of the core distance from the wall. The curves displayed in Fig. 4 show the values of $d_e(z)$ normalized by the length of fully stretched ligands, $D_N = (N-1)\sigma$.

Surprisingly, for a given type of molecules, the dependence of $d_e(z)$ on the distance from the wall is very weak. Close to the wall a small minimum and following it a small maximum appear. The values $d_e(z)$ are slightly larger at lower bulk density. This effect is quite obvious since for bulk systems the molecules are more coiled at higher densities.

The normalized end-to-end distances are larger for shorter ligands, i.e., for longer ligands, an increase of tendency to coiling is observed.

We have also evaluated the mass dipoles and their length and orientation with respect to the vector perpendicular to the wall in functions of the core distance from the wall. These characteristics provide information about nonuniformity of the distribution of segments around core particles. In Fig. 5, we show the normalized histograms $P(R_m)$ of the lengths R_m of the mass dipoles at two distances of core molecules from the wall. Note that in all cases the length of mass dipoles is somewhat lower if the core molecule is adjacent to the wall, compared to the core molecule in the bulk part of the system. The plots presented here are characteristic for other bulk densities.

An increase of the bulk density causes the shift of the histograms towards lower values of R_m. This point illustrates

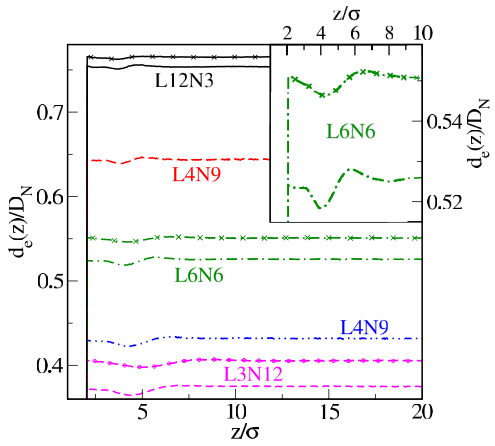

FIG. 4. The end-to-end distances normalized by the length of stretched chains, $D_N = (N-1)\sigma$. Lines are for the systems from Fig. 1(a), while lines decorated with symbols – for selected systems from Fig. 1(b). The inset magnifies the results for the systems $L6N6$ at distances close to the wall.

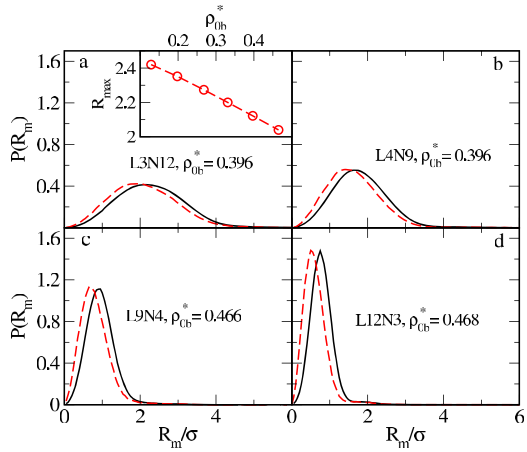

FIG. 5. Normalized distributions of the lengths of the mass dipoles, $P(R_m)$, for selected systems. The bulk densities ρ^*_{0b} are given in the figure. Dashed red lines are for the core particles located at the wall, $z = 2\sigma$, while solid black lines—at $z = 10\sigma$. The inset of (a) illustrates how the location of the maximum of $P(R_m)$ at $z = 2\sigma$ changes with the bulk density ρ^*_{0b}. These calculations are for the system $L3N12$.

the inset of panel (a), where we show how the position of the maximum of $P(R_m)$ changes with the bulk density in the system $L3N12$. This plot is a characteristic also for other systems. As one can expect, the length of the mass dipoles increases for increasing number of segments per ligand, N. Also, the Gaussian-like histograms become broader for larger N. Note that all plots in Fig. 5 have been drawn using the same scale. The obtained results for the length of the mass dipoles are not surprising: more significant nonuniformity in the distribution of segments around cores occurs for longer (and instantaneously fewer) ligands.

Normalized probability densities $P(t)$, $(t = \cos\theta)$, characterizing orientation of the mass dipoles for selected systems and at selected distances of the core particle from the wall, are displayed in Figs. 6(a) and 6(b). Before interpreting those curves we recall that for $\theta = 0$ $(t = 1)$ the majority of the segments is concentrated at the hemisphere of the core opposite to the wall, for $\theta = \pi/2$ $(t = 0)$ the mass dipoles are parallel to the wall, and for $\theta = \pi$ $(t = -1)$ the mass dipole vector points toward the wall. In general, for the cores from the layer adjacent to the wall, the orientation effects are more pronounced for systems with shorter ligands and weaker for longer ligands. However, for longer ligands, the orientation effects extend over larger distances from the wall.

Let us compare the distributions $P(t)$ for two extreme cases of $L3N12$ (upper left panel) and of $L12N3$ [lower right panel of Fig. 6(a)]. In the first ($L3N12$) case, the dipoles for the layer of cores adjacent to the wall ($z = 2\sigma$) predominantly assume their orientation parallel to the wall, although many of them posses orientation with $0 < \theta < \pi/2$. This predominant orientation ($\theta = 0$) extends over several layers and even at $z = 10\sigma$ some marginal effects are seen. In the second case ($L12N3$, lower right panel), the function $P(t)$ of mass dipoles for the cores adjacent to the wall exhibits a large maximum at $\theta = 0$, but orientation effects vanish quickly with z. Moreover, at moderate bulk fluid density the orientation effects within the cores at the wall are more pronounced than at high density [Fig. 6(b)], but they disappear quickly with z and at

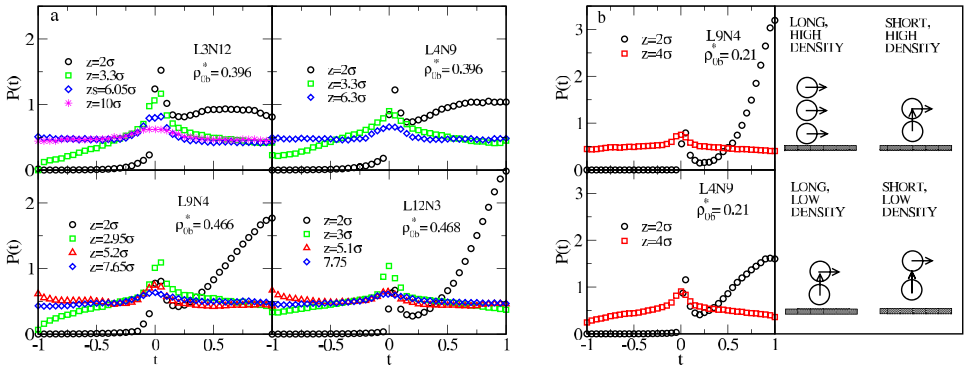

FIG. 6. Examples of the distribution functions $P(t)$ illustrating the orientation of mass dipoles. Particular panels have been obtained for systems that differ by the numbers of the ligands, L, and of the segments, N. Different curves, however, correspond to different locations of the core with respect to the wall, z. In (a), these locations are just consecutive maxima and minima of the local densities $\rho_0(z)$, cf. Fig. 1. Part (a) is for high bulk densities, while part (b)—for moderate bulk densities. Right panel of (b) illustrates schematically how the dominating orientation in consecutive layers changes with the length of ligands and bulk density.

$z = 4\sigma$ only marginal ordering with small maxima at $\theta = \pi/2$ is seen.

Right panel of Fig. 6(b) displays schematic predominant ordering within consecutive maxima of the local density $\rho_0(z)$. For long chains at high bulk density, the mass dipoles within consecutive layers of cores are oriented parallel to the surface. For long as well as short chains at lower bulk densities and for short chains at high bulk densities, the dipoles for the cores adjacent to the wall possess predominant orientation with $\theta = 0$ and $\theta = \pi/2$ for the next layers. Physical interpretation of the sources of the observed differences in the behavior of different systems is difficult. Perhaps, more detailed answers could be found by introducing some additional characteristics, like the components of the "local" gyration tensor, dependent on the distance of a particle from the wall. A fast decay of the orientational effects is also connected with the assumed repulsive wall-core and wall-segment forces and purely repulsive segment-segment interactions. For the systems with attractive wall-segment and segment-segment interactions, one can expect a spontaneous reorganization ("patterning") within segments around a single nanoparticle.[19] The reorganization of the segments would result in the changes of the mass dipole. This effect could depend on the distance of the core from the wall, due to a competition between wall-segment and segment-segment interactions.

Figure 7 displays examples of the radial distribution function of the cores for two limiting with respect to the number of ligands systems, namely, for $L3N12$ and for $L12N3$ at a high and at a moderate bulk density. For each case, two radial distribution functions have been evaluated for the layer of 1σ thick parallel to the wall and passing through the first local density maximum (cf. Fig. 1) and for the layer of the same thickness in the bulk part of the system. Of course, in the bulk phase, the pair correlations are much less pronounced, due to lower average density within that layer. Note that the plots of pair correlation functions for remaining system at similar bulk densities "lie between" the functions from Fig. 7.

Similarly as in the case of core local densities, the oscillations of radial distributions are more pronounced for the systems with shorter ligands, i.e., on average, shorter ligands are a bigger obstacle for proximity of cores to nearer distances. For longer ligands, the pair correlations are much less pronounced and for the system $L3N12$ at high bulk density only one peak for the first correlation shell is seen in Fig. 7. Moreover, for the system $L12N3$, the distance between the consecutive peaks of $g(r)$ is larger than 5σ, i.e., it is significantly higher than the Lennard-Jones diameter of cores σ_0. Our general observation is that at constant N_t the presence of short ligands strengthens core-core and core-wall correlations, while long ligands—weaken those correlations.

The results for the radial distribution function, together with the results for the core local densities, suggest quite different influence of short and long ligands on the structure of the fluid. In other words, the structural properties of the systems strongly depend on architecture of particles. If we employ a perturbation approach to the system excess (over an ideal system) free-energy, then the only free-energy term that explicitly depends on the number of core-segment and segment-segment bonds is the term due the intramolecular connectivity and this term has a dominant influence of the observed structural differences.

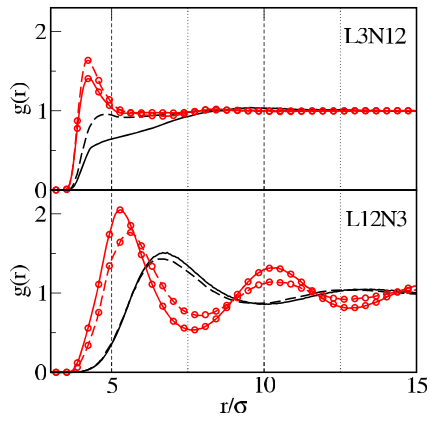

FIG. 7. Examples of the pseudo-two-dimensional radial distribution functions for the system $L3N12$ (upper panel) and $L12N3$ (lower panel). Lines decorated with symbols denote the functions at the surface (within the first local density maximum), while lines without symbols are the functions in the bulk part of the systems. Solid lines correspond to high bulk density, $\rho^*_{0b} = 0.468$ and dashed lines—to moderate bulk densities, $\rho^*_{0b} = 0.211$.

We have also evaluated effective particle-particle interactions between a pair of particles. In contrast to the previous studies,[30] in this study we have computed the "Boltzmann averaged" potential (that, in fact, is identical with the pair potential used in the Reference Average Mayer theory of molecular fluids[58,59]). We calculated the bulk radial distribution functions at two very low bulk densities and extrapolated them to zero bulk density. Then, the effective potential was

$$U_{eff}(r) = -kT \ln G_2(r), \tag{7}$$

where $G_2(r) = \lim_{\rho_{0b}\to 0} g(r)$.

The potential $U_{eff}(r)$ for investigated systems is shown in Fig. 8. Additionally, we have evaluated the effective Barker-Henderson diameter,[60] $d_{eff} = D_{eff}/\sigma$,

$$D_{eff} = \int_0^{R_0} dr\{1 - \exp[-U_{eff}(r)/kT]\}, \tag{8}$$

where R_0 is the root of $U_{eff}(R_0) = 0$. The dependence of d_{eff} on the number of ligands is displayed in the inset of Fig. 8.

Except for the system $L12N3$ (and, to a small extent, for the system $L9N4$), where at some core-core separations a very weak attractive well appears, the effective potentials are repulsive. Of course, this attractive well is due to direct core-core interactions. Instantaneously, the repulsive branch of the effective potential for the systems $L12N3$ and $L9N4$ is "harder" than for all remaining systems. With a decrease of L (i.e., with an increase of N), the repulsive branches become "softer," but the range of the repulsion increases. The effective potential decays to zero at the distance $r = 2d + 2(N-1)\sigma$.

Although differences between the effective potential for particular systems are significant, the differences between values of d_{eff} are not so big. The effective Barker-Henderson diameter ranges from approximately 5.95σ to 6.2σ and the largest value of d_{eff} is observed, surprisingly, for longest, $N = 12$, ligands.

In perturbation theories of simple fluids, the effective Barker-Henderson diameter is usually treated as the diameter of the reference, hard-sphere system. The effective reduced density of such reference system would be thus larger for higher values of d_{eff}, thus oscillations of the relevant pair distribution function would be expected to be larger, contrary to the simulation results. The mobility of ligands depends on the system density. This means that the effective potential obtained in zero-density limit cannot be used to approximate core-core interactions in more dense systems. Thus, "effective diameter" in a hypothetical perturbation theory for considered systems should be also strongly density dependent.

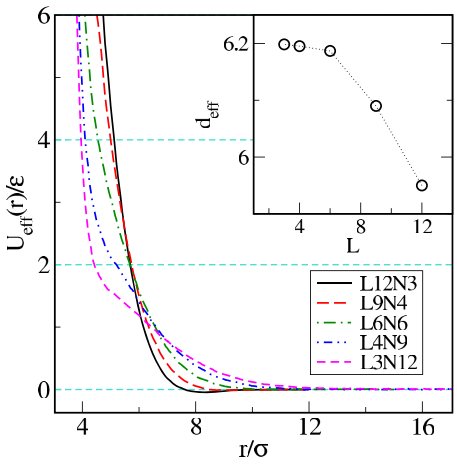

FIG. 8. The effective pair potential $U_{eff}(r)$ for the systems described in the figure. The inset illustrates how the Barker-Henderson diameter, d_{eff}, changes with the number of ligands, L, at $L \times N = 36$.

IV. DENSITY FUNCTIONAL THEORY

A. The theory

We have undertaken efforts to describe local densities by means of a version[44,49] of density functional theory. This approach is a quite standard now, and we outline its basic points only. First, we concentrate on the principal model difference between the theory and simulations. In contrast to simulations, the length of the bonds in the theory is assumed to be constant, while in simulations the bond length can fluctuate and the range of these fluctuations depends on the force constants in Eqs. (1) and (2). In theory, the intramolecular bonding potential, $V_b(\mathbf{R})$, has the form[44,49]

$$\exp[-V_b(\mathbf{R})/kT] = \prod_{i=1}^{L} \frac{\delta(|\mathbf{r}_0 - \mathbf{r}_1^{(i)}| - d)}{4\pi d^2} \times \prod_{j=1}^{N-1} \frac{\delta(|\mathbf{r}_j^{(i)} - \mathbf{r}_{j+1}^{(i)}| - \sigma)}{4\pi\sigma^2}. \tag{9}$$

In the above, $\mathbf{R} = (\mathbf{r}_0, \{\mathbf{r}_j^{(i)}\})$, the superscript refers to the ligand $i = 1, 2, \ldots, L$, and the subscript—to the segment number $j = 1, 2, \ldots, N$.

The grand potential of the system, Ω, is a functional of the local density of particles, $\rho(\mathbf{R})$,

$$\Omega[\rho(\mathbf{R})] = F_{id}[\rho(\mathbf{R})] + F_{ex}[\rho(\mathbf{R})] + \int d\mathbf{R}[V_{ext}(\mathbf{R}) - \mu]\rho(\mathbf{R}). \tag{10}$$

In the above, μ is the configurational chemical potential, $V_{ext}(\mathbf{R})$ is the external potential field, being the sum of the external potential energies acting on the core and all the segments,

$$V_{ext}(\mathbf{R}) = v_0(\mathbf{r}_0) + \sum_{i=1}^{L}\sum_{j=1}^{N} v_s(\mathbf{r}_j^{(i)}), \tag{11}$$

$F_{id}[\rho(\mathbf{R})]$ is the ideal free-energy, $F_{id}[\rho(\mathbf{R})]/kT = \int d\mathbf{R}\rho(\mathbf{R})[V_b(\mathbf{R}) + \ln(\rho(\mathbf{R})) - 1]$, and $F_{ex}[\mathbf{R}]$ is the excess free-energy.

The excess free-energy of the system is decomposed into the following parts: hard-sphere, F_{hs}, attractive force, F_{att}, and the contribution due to intramolecular connectivity, F_b, $F = F_{hs} + F_{att} + F_b$. In order to write down these functionals, we introduce the site densities for all the sites of the particle. The symbol $\rho_0(z)$ abbreviates the core local density and $\rho_j^{(i)}(z)$, the density of jth segment within the ith ligand. For the model in question, the functions $\rho_j^{(i)}(z)$ are independent of the ligand's number. We also introduce the total densities: the total segment density, $\rho_s(z)$, $\rho_s(z) = \sum_{j=1}^{N}\rho_j(z)$, $\rho_j(z) = L\rho_j^{(i)}(z)$, and the total density of all sites $\rho_t(z) = \rho_0(z) + \rho_s(z)$.

The excess free-energies F_{hs} and F_b are evaluated[44,49] by using an approach that requires the introduction of four scalar and two vector weighted densities and the White-Bear theory

for the free energy of hard spheres.[50,51] The definitions of the scalar weighted densities, $n_\alpha(\mathbf{r})$, $\alpha = 0, 1, 2, 3$, as well as the two vector densities, $\mathbf{n}_{V\gamma,m}(\mathbf{r})$, $\gamma = 1, 2$, together with the definition of F_{hs} can be found in several studies[44,49–51] and for this reason we have decided to omit is here. We only mention that in our treatment the diameters of hard spheres of cores and of segments have been set to the Lennard-Jones diameters σ_0 and σ, respectively.

The attractive van der Waals interactions appear only between the cores. Assuming mean-field approximation, the free energy resulting from attractive intermolecular forces is

$$F_{att}[\rho(\mathbf{R})] = \frac{1}{2}\left\{\int d\mathbf{r}_0 \rho_0(\mathbf{r}_0) \int d\mathbf{r}_0' \rho_0(\mathbf{r}_0') u_{00}^{(att)}(|\mathbf{r}_0 - \mathbf{r}_0'|)\right\}, \tag{12}$$

where the attractive part, $u_{00}^{(att)}$, of the potential (3) is defined according to the Barker-Henderson approach,

$$u_{kl}^{(att)}(r) = \begin{cases} 0, & r < \sigma_{kl}, \\ u_{kl}(r), & \text{otherwise.} \end{cases} \tag{13}$$

We are aware that more sophisticated treatments exist, but since we employ the theory to the systems at temperature much higher than the bulk critical temperature, we have decided to employ this simplest division.

The free-energy contribution due to the intramolecular connectivity is approximated by the expression resulting from Wertheim's theory of association, generalized[44,49,52] to nonuniform fluids

$$F_b/kT = \int d\mathbf{r}\left[\frac{L - LN}{LN + 1} n_0(\mathbf{r})\xi(\mathbf{r}) \ln y_{hs}(\sigma, \sigma, \{n_\alpha\}) - \frac{L}{LN + 1} n_0(\mathbf{r})\xi(\mathbf{r}) \ln y_{hs}(\sigma, \sigma_0, \{n_\alpha\})\right], \tag{14}$$

where $\xi(\mathbf{r}) = 1 - \mathbf{n}_{V2}(\mathbf{r}) \cdot \mathbf{n}_{V2}(\mathbf{r})/n_2^2(\mathbf{r})$ and $\ln y_{hs}(\sigma, \sigma, \{n_\alpha\})$ and $\ln y_{hs}(\sigma, \sigma_0, \{n_\alpha\})$ are the contact values of the hard-sphere cavity functions, i.e., the values of $y(s, s_1, \{n_\alpha\})$ at the distance $(s + s_1)/2$ and they are given by Eq. (11) of Ref. 49.

The density profile equations are obtained minimizing the grand canonical potential, $\delta\Omega/\rho(\mathbf{R}) = 0$. For the system with local densities varying in one dimension, z, we obtain

$$\rho_0(z) = \exp(\mu/kT) h_0(z) [G^{(N+1)}(z)]^L \tag{15}$$

and

$$\rho_j^{(i)}(z) = \exp(\mu/kT) h_j^{(i)}(z) G^{(N+1-j)}(z) \tilde{G}^{(j+1)}(z), \tag{16}$$

where $h_j^{(i)}(z) = \exp\left\{-[\delta F_{ex}/\delta\rho_j^{(i)}(z) + v_s(z)]/kT\right\}$, $h_0 = \exp\{-[\delta F_{ex}/\delta\rho_0(z) + v_0(z)]/kT\}$. We recall that according to our model the functions $h_j^{(i)}$ are independent of the ligand index i; thus we can drop the superscript (i) in the symbols of these functions, $h_j \equiv h_j^{(i)}$. The functions $G^{(j)}$ and $\tilde{G}^{(j)}$ are given by the following recurrence relations:

$$G^{(j)}(z) = \int dz' h_{N-j+2}(z') \frac{H(d_{N-j} - |z - z'|)}{2d_{N-j}} G^{(j-1)}(z'), \tag{17}$$

for $j = 2, 3, \ldots, N$ and $G^{(1)}(z) \equiv 1$,

$$\tilde{G}^{(2)}(z) = \int dz h_0(z') \frac{H(d_0 - |z - z'|)}{2d_0} [G^{(N+1)}(z')]^{L-1}, \tag{18}$$

and, for $j > 2$,

$$\tilde{G}^{(j)}(z) = \int dz h_j(z') \frac{H(d_j - |z - z'|)}{2d_j} \tilde{G}^{(j-1)}(z'). \tag{19}$$

In the above, $H(d - z)$ is the step-function and $d_0 = d$ and $d_j = \sigma$ for $j = 2, 3, \ldots, N$. Details on the numerical methods are given in Refs. 44 and 49.

The above equations are analogous to those developed for star polymers.[44,49] However, in the case of star polymers, the geometry of "tethering points" is usually fixed. The fixed molecular geometry can be taken into account employing the second-order Wertheim theory for the free-energy contribution due to intramolecular bonding[44] or alternatively by imposing angular bonds and angular-dependent bonding potential, cf. Eq. (7) of Ref. 49. The model considered here assumes that the ligands can "slide" over the core surface, consequently the geometry of particles changes. This justifies the application of the first-order Wertheim theory.

The architecture of particles enters explicitly the density profile equations at two places. First, the expression for F_b [Eq. (14)] and thus the functions $h_0(z)$ and $h_j(z)$ depend on N and L and on $y(s, s_1, \{n_\alpha\})$. Second, structure of the recurrence relations (17)–(19) results from the form of the binding potential (9), i.e., from the number of ligands L and the number of segments per ligand, N.

B. Comparisons with simulation data

In numerical calculations we have used the fast Fourier transform method to calculate the convolution integrals and the grid size equal to 0.02σ. In principle, the method of numerical calculations was quite similar to the methods employed in Refs. 44 and 49.

The principal aim of our calculations is to check the quality of the predictions of the theory for different systems under study. The self-consistency and accuracy of calculations was checked through the pressure sum rule, which states that the system pressure is equal to the sum of the local densities of cores and segments in contact with the wall, $p/kT = \rho_0(z = \sigma_0/2) + \rho_s(z = \sigma_s/2)$. Comparing this value to the bulk pressure computed from the grand potential for bulk system yields a measure of self-consistency. The agreement was quite good and is of the order of 0.5%, in general. It is not surprising, since DFT is constructed so that this sum rule is satisfied.[44]

In Fig. 9, we compare the density profiles for the system *L6N6* obtained from simulations (symbols) and from theory.

In the case of the system with small number of long ligands, the agreement of theory with simulations is quite satisfactory. Similarly as in the case of polymeric systems (cf. Ref. 38 and the references quoted therein), it is somewhat better at higher bulk densities, and better for core (larger) than for segment (smaller) densities.

In the case of the profiles of segments [(b) and (d)], the cusps appear $z/\sigma = 1.5$. The origin of the cusps is the same as the origin of the cusps in the profiles of the tethered layer at a wall:[61] the existence of bonds. In particular, the cusp at $z/\sigma = 1.5$ results from configurations where one segment is at the distance of the closest approach from the

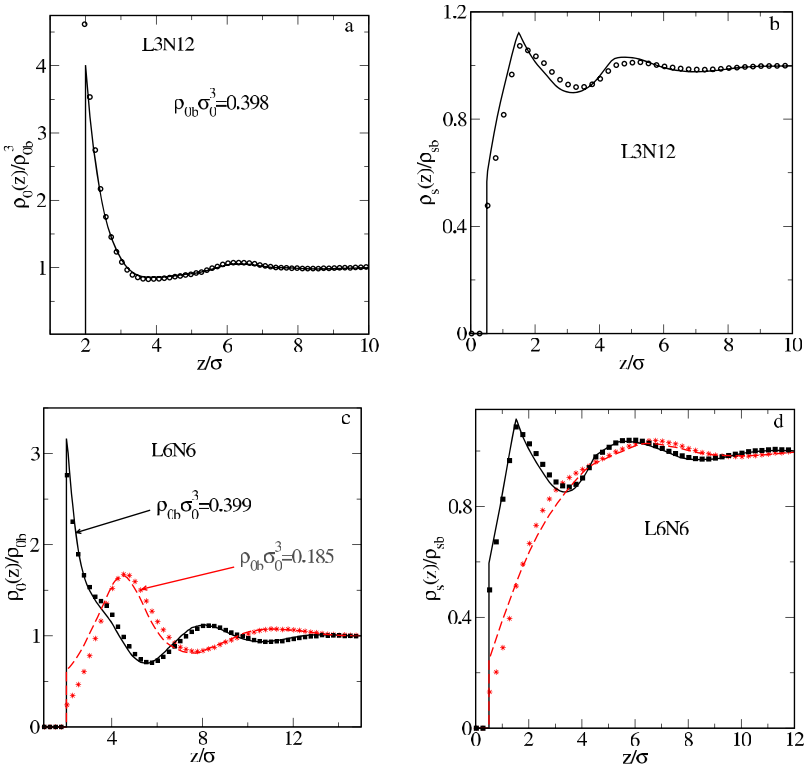

FIG. 9. Comparisons of the local densities of cores [(a) and (c)] and segments [(b) and (d)] for the systems $L3N12$ [(a) and (b)] and $L6N6$ [(c) and (d)] at bulk core densities given in (a) and (c) [the bulk core densities in (b) are the same as in (a), and in (d)—the same as in (c)]. Symbols are simulation results and lines are theoretical predictions. For clarity, in the case of simulation data only every four have been plotted.

wall while its neighboring segment is located perpendicularly to the wall at the bonding distance from the first one. For the profiles evaluated from the theory, these cusps are well-seen, and in the case of simulated data, they are slightly rounded off, due to small fluctuations of the lengths of bonds between segments.

If the number of ligands increases, the agreement of theoretical predictions becomes worse. We have concentrated on the profiles of the cores and Fig. 10 compares the results obtained for the systems $L9N4$ and $L3N12$ at rather high bulk density, $\rho_0^* = 0.466$. The theory predicts the simulation data at a quantitative level. In particular, for the system $L9N4$, the course of $\rho_0(z)$ at the wall as predicted by the theory significantly deviates from the simulation result. Similar observation concerns the system $L3N12$, but not also the simulated and theoretical density are slightly shifted in phases.

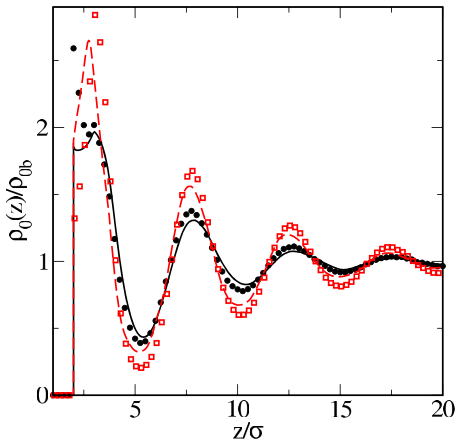

FIG. 10. Comparisons of the local densities of cores for the systems $L9N4$ (black solid line and circles) and $L12N3$ (red dashed line and square). Symbols are simulation results and lines are theoretical predictions. For clarity, in the case of simulation data only every four have been plotted. For both systems, the bulk core density is 0.466.

Assessing significance of the above results, one should recall differences between models used in theory and simulations. Whereas theory assumes constant lengths of all bonds and hard-core segments in simulations, the lengths of bonds fluctuate and the segments are "soft," as their mutual interactions are described by the repulsive branch of the Lennard-Jones (12,6) potential. It is not clear if those differences in the calculation procedure lead to reduction or enlargement of the errors of theoretical procedure.

Our conclusions arising from the latter calculations are that the DFT seems to provide reasonable results if the number of attached ligands is not very high. For a big number of ligands, the system resembles the so-called Gaussian-hard core model that was used to describe star polymers by means of a density functional approach.[62,63] This type of model is based on the development of an effective particle-particle potential $U_{eff}(r)$.

V. SUMMARY

In this work, we have carried out large scale molecular dynamics simulations of systems involving particles with a number of mobile ligands attached to the cores in contact with a hard wall. Our calculations have been performed assuming that the total number of segments is constant. Moreover, our calculations are based on an implicit solvent model, that is, no solvent molecules are present in the system, but the interactions should be treated as effective, solvent mediated ones. Despite the above simplification, the simulated

systems comprised hundreds of thousands of "atomic units" (i.e., segments and cores). Segment-segment and segment-core interactions were purely repulsive, while the core-core interactions were described by Lennard-Jones (12,6) potential. Therefore, the interactions between segments effectively screen direct core-core attractions.

For all systems, we evaluated local densities of cores and of segments. The shape of the density profiles crucially depends on the number of ligands. If the number of ligands increases (i.e., if the number of segments per ligand decreases), the structure of the fluid at the wall becomes more pronounced and for the shortest ligands (the system $L12N3$) the density profile exhibits the existence of a well-developed layered structure that extends over 5-6 layers from the wall. By contrast, in the systems with long ligands, the density profiles exhibit only one pronounced peak at the wall and the layered structure decays quickly with the distance from the surface. We have also evaluated the Boltzmann averaged effective particle-wall potentials. Of course, these potentials are soft repulsive and their range depends on the number of ligands per segment.

The structure of the fluid within slabs parallel to the wall was characterized by the pseudo-two-dimensional core-core radial distribution functions. The change of the shape of these functions with the number of ligands L is similar as the change of the density profiles. Larger number of short ligands results in a significant increase of the pair correlations. Except for the systems $L12N3$, the effective, Boltzmann averaged pair potentials are repulsive, i.e., the screening of direct, attractive core-core interactions by the repulsive segment-segment and segment-core ones is effective for the majority of the investigated systems. Even for the system $L12N3$, the attractive well of the effective pair potential is very shallow.

The distribution of segments around cores was characterized by end-to-end distances and by the lengths and orientations of the mass dipoles. We investigated how these characteristics vary with the distance of cores from the wall. Surprisingly, the end-to-end distances of ligands are almost insensitive to the position of cores with respect to the wall. Similarly, the dependence of the lengths of the mass dipoles on the location of the core molecules is weak. The mass dipoles are slightly longer for the molecules located in the bulk part of the systems. The orientation of the mass dipoles depends on the number (length) of the ligands and on the bulk density. For low bulk densities and for longer ligands, the orientation of the mass dipoles for cores adjacent to the wall is perpendicular to the wall with ligands grouped at the hemisphere of the core directed toward the system interior. Under a similar bulk density the mass dipoles of the cores at the wall for short ligands are oriented parallel to the wall. For high densities, the cores adjacent to the wall with short, as well as with long ligands the mass dipoles assume orientations parallel to the wall. Except for high bulk densities, the orientation effects decay quickly with the distance of cores from the wall.

In order to describe the density profiles have also used a version of the density functional approach. The theory employed by us was previously used for the description of star polymers. For the systems composed of particles with $3 \leq L \leq 6$ ligands this theory for the profiles of cores works reasonable well at higher densities and larger deviations are observed only low values of ρ_{0b}. However, for the systems with $L = 9$ and $L = 12$, the discrepancies between theory and simulations are more significant. The systems with high number of ligands resemble the systems involving hard-core Gaussian overlap molecules. The latter systems have been previously described using appropriate effective pair potentials.

In our opinion, it would be of interest to extend the present study to the case of hairy molecules confined between two hard walls (in slit-like pores). The presence of two walls located nearby should lead to more pronounced differences between investigated models due to additional strong geometrical constrains. The investigation of the behavior of nanoparticles in pores would be useful to explain some phenomena that occur during flow of mixtures of fluids and nanoparticles.[64,65] Moreover, adsorption of nanoparticles on surfaces can change their wettability[66,67] and density functional approach is well suited to study surface phase transitions. Some of those problems are currently under study in our laboratory.

ACKNOWLEDGMENTS

S.S. and T.S. acknowledge support from NCN Poland under Grant No. 2015/17/B/ST4/03615.

[1] X. Tian, H. Zheng, and U. Mirsaidov, "Aggregation dynamics of nanoparticles at solid–liquid interfaces," Nanoscale **9**, 10044 (2017).
[2] E. Miele, S. Raj, Z. Baraissov, P. Král, and U. Mirsaidov, "Dynamics of templated assembly of nanoparticle filaments within nanochannels," Adv. Mater. **29**, 1702682 (2017).
[3] S. W. Chee, Z. Baraissov, N. D. Loh, P. T. Matsudaira, and U. Mirsaidov, "Desorption-mediated motion of nanoparticles at the liquid–solid interface," J. Phys. Chem. C **120**, 20462 (2016).
[4] S. A. Vasudevan, A. Rauh, L. Barbera, M. Karg, and L. Isa, "Stable in bulk and aggregating at the interface: Comparing core-shell nanoparticles in suspension and at fluid interfaces," Langmuir **34**, 886 (2018).
[5] P. Hanarp, D. S. Sutherland, J. Gold, and B. Kasemo, "Influence of polydispersity on adsorption of nanoparticles," J. Coll. Interface Sci. **241**, 26 (2001).
[6] J. Lu, D. Liu, X. Yang, Y. Zhao, H. Liu, H. Tang, and F. Cui, "Molecular dynamics simulations of interfacial interactions between small nanoparticles during diffusion-limited aggregation," Appl. Surf. Sci. **357**, 1114 (2015).
[7] J. Che, A. Jawaid, C. A. Grabowski, Y.-J. Yi, G. C. Louis, S. Ramakrishnan, and R. A. Vaia, "Stability of polymer grafted nanoparticle monolayers: Impact of architecture and polymer–substrate interactions on dewetting," ACS Macro Lett. **5**, 1369 (2016).
[8] A. Maestro, E. Guzmán, F. Ortega, and R. G. Rubio, "Contact angle of micro-and nanoparticles at fluid interfaces," Curr. Opin. Colloid Interface Sci. **19**, 355 (2014).
[9] J. Reguera, E. Ponomarev, T. Geue, F. Stellacci, F. Bresme, and M. Moglianetti, "Contact angle and adsorption energies of nanoparticles at the air-liquid interface determined by neutron reflectivity and molecular dynamics," Nanoscale **7**, 5665 (2015).
[10] S. Crossley, J. Faria, M. Shen, and D. E. Resasco, "Solid nanoparticles that catalyze biofuel upgrade reactions at the water/oil interface," Science **327**, 68 (2010).
[11] A. Verma and F. Stellacci, "Effect of surface properties on nanoparticle-cell interactions," Small **6**, 12 (2010).
[12] A. Böker, J. He, T. Emrick, and T. P. Russell, "Self-assembly of nanoparticles at interfaces," Soft Matter **3**, 1231 (2007).

[13]J. Wang, P. Kanjanaboos, S. P. McBride, E. Barry, X.-M. Lin, and H. M. Jaeger, "Mechanical properties of self-assembled nanoparticle membranes: Stretching and bending," Faraday Discuss. **181**, 325 (2015).
[14]J. He, X.-M. Lin, H. Chan, L. Vukovi, P. Kral, and H. M. Jaeger, "Diffusion and filtration properties of self-assembled gold nanocrystal membranes," Nano Lett. **11**, 2430 (2011).
[15]P. Akcora, H. Liu, S. K. Kumar, J. Moll, Y. Li, C. Benicewicz, L. S. Schadler, D. Acehan, A. Z. Panagiotopoulos, V. Prymatsyn, V. Ganesan, J. Ilavsky, P. Thiyagarajan, R. H. Colby, and J. F. Douglas, "Anisotropic self-assembly of spherical polymer-grafted nanoparticles," Nat. Mater. **8**, 354 (2009).
[16]M. K. Corbierre, N. S. Cameron, M. Sutton, K. Laaziri, and R. B. Lennox, "Gold nanoparticle/polymer nanocomposites: Dispersion of nanoparticles as a function of capping agent molecular," Langmuir **21**, 6063 (2005).
[17]S. Kinge, M. Crego-Calama, and D. N. Reinhoudt, "Self-assembling nanoparticles at surfaces and interfaces," Chem. Phys. Phys. Chem. **9**, 20 (2008).
[18]M. G. Moffitt, "Self-assembly of polymer brush-functionalized inorganic nanoparticles: From hairy balls to smart molecular mimics," J. Phys. Chem. Lett. **4**, 3654 (2013).
[19]P. Pengo, M. Sologan, L. Pasquato, F. Guida, S. Pacor, A. Tossi, F. Stellacci, D. Marson, S. Boccardo, S. Pricl, and P. Posocco, "Gold nanoparticles with patterned surface monolayers for nanomedicine: Current perspectives," Eur. Biophys. J. **46**, 749 (2017).
[20]P. Ohlendorf, M. Dulle, S. Förster, and A. Greiner, "Supramolecular nanocomposites: Dual-functional cholesteric hydroxypropyl cellulose esters chemically linked to gold nanoparticles," ChemNanoMat **2**, 290 (2016).
[21]M. Bagiński, A. Szmurło, A. Andruszkiewicz, M. Wójcik, and W. Lewandowski, "Dynamic self-assembly of nanoparticles using thermotropic liquid crystals," Liq. Cryst. **43**, 2391 (2016).
[22]N. J. Fernandes, H. Koerner, E. P. Giannelis, and R. A. Vaia, "Hairy nanoparticle assemblies as one-component functional polymer nanocomposites: Opportunities and challenges," MRS Commun. **3**, 13 (2013).
[23]E. Bianchi, B. Capone, G. Kahl, and C. N. Likos, "Soft-patchy nanoparticles: Modeling and self-organization," Faraday Discuss. **181**, 123 (2015).
[24]I. C. Gârlea, E. Bianchi, B. Capone, L. Rovigatti, and C. N. Likos, "Hierarchical self-organization of soft patchy nanoparticles into morphologically diverse aggregates," Curr. Opin. Colloid Interface Sci. **30**, 1 (2017).
[25]*Self-Assembling Systems: Theory and Simulation*, edited by L.-T. Yan (John Wiley & Sons, Ltd., Chichester, UK, 2017), ISBN: 978-1-119-11314-0.
[26]K. H. Ku, Y. J. Kim, G.-R. Yi, Y. S. Jung, and B. J. Kim, "Soft patchy particles of block copolymers from interface-engineered emulsions," ACSNano **9**, 11333 (2015).
[27]J. M. Ilnytskyi, A. Slyusarchuk, and M. Saphiannikova, "Photocontrollable self-assembly of azobenzene-decorated nanoparticles in bulk: Computer simulation study," Macromolecules **49**, 9272 (2016).
[28]J. M. Ilnytskyi, A. Slyusarchuk, and M. Saphiannikova, "Photocontrollable percolation of decorated nanoparticles in a nanopore: Molecular dynamics simulation study," Math. Model. Comput. **3**, 33–42 (2016), http://ena.lp.edu.ua.
[29]M. S. Nikolic, C. Olsson, A. Salcher, A. Kornowski, A. Rank, R. Schubert, A. Froemsdorf, H. Weller, and S. Foerster, "Micelle and vesicle formation of amphiphilic nanoparticles," Angew. Chem., Int. Ed. **48**, 2752 (2009).
[30]Ł. Baran and S. Sokołowski, "Effective interactions between a pair of particles modified with tethered chains," J. Chem. Phys. **147**, 044903 (2017).
[31]L. Carbone, L. Manna, and C. Soennichsen, "Self-assembly of amphiphilic nanocrystals," Angew. Chem., Int. Ed. **48**, 4282 (2009).
[32]M. Borówko, W. Rżysko, S. Sokołowski, and T. Staszewski, "Phase behavior of decorated soft disks in two dimensions," J. Chem. Phys. **145**, 224703 (2016).
[33]S. A. J. van der Meulen and M. E. Leunissen, "Solid colloids with surface-mobile DNA linkers," J. Am. Chem. Soc. **135**, 15129–15134 (2013).
[34]S. A. J. van der Meulen, G. Helms, and M. Dogterom, "Solid colloids with surface-mobile linkers," J. Phys.: Condens. Matter **27**, 233101 (2015).
[35]W. B. Rogers, W. M. Shih, and V. N. Manoharan, "Using DNA to program the self-assembly of colloidal nanoparticles and microparticles," Nat. Rev. Mater. **1**, 1–14 (2016).
[36]V. Ganesan and A. Jayaraman, "Theory and simulation studies of effective interactions, phase behavior and morphology in polymer nanocomposites," Soft Matter **10**, 13 (2014).
[37]J. Wu and Z. Li, "Density-functional theory for complex fluids," Annu. Rev. Phys. Chem. **58**, 85 (2007).
[38]A. Patrykiejew, O. Pizio, and S. Sokołowski, "Statistical surface thermodynamics," in *Surface and Interface Science: Solid-Gas Interfaces II*, edited by K. Wandelt (Wiley-VCH Verlag GmbH & Co. KGaA, Weinheim, Germany, 2016), Vol. 6, pp. 883–1253.
[39]J. Jiang and D. Cao, "Modeling of highly efficient drug delivery system induced by self-assembly of nanocarriers: A density functional study," Sci. China Chem. **56**, 249 (2012).
[40]E. Sauer and J. Gross, "Classical density functional theory for liquid–fluid interfaces and confined systems: A functional for the perturbed-chain polar statistical associating fluid theory equation of state," Ind. Eng. Chem. Res. **56**, 4119 (2017).
[41]C. Chen, P. Tang, F. Qiu, and A.-C. Shi, "Density functional study for homodendrimers and amphiphilic dendrimers," J. Phys. Chem. B **120**, 5553 (2016).
[42]P. Cremer, M. Heinen, A. M. Menzel, and H. Löwen, "A density functional approach to ferrogels," J. Phys.: Condens. Matter **29**, 275102 (2017).
[43]M. Marechal, S. Dussi, and M. Dijkstra, "Density functional theory and simulations of colloidal triangular prisms," J. Chem. Phys. **146**, 124905 (2017).
[44]A. Malijevský, P. Bryk, and S. Sokołowski, "Density functional approach for inhomogeneous star polymer fluids," Phys. Rev. E **72**, 032801 (2005).
[45]D. Cao, T. Jiang, and J. Wu, "A hybrid method for predicting the microstructure of polymers with complex architecture: Combination of single-chain simulation with density functional theory," J. Chem. Phys. **124**, 164904 (2006).
[46]E. S. McGarrity, J. M. Thijssen, and N. A. M. Besseling, "Fluids density functional theory studies of supramolecular polymers at a hard surface," J. Chem. Phys. **133**, 084902 (2010).
[47]B. D. Marshall and W. G. Chapman, "Higher order classical density functional theory for branched chains and rings," J. Phys. Chem. B **115**, 15036 (2011).
[48]J. Jiang, X. Xu, and D. Cao, "Density functional theory for inhomogeneous ring polymeric fluids," Phys. Rev. E **86**, 041805 (2012).
[49]J. Jiang, X. Xu, J. Huang, and D. Cao, "Density functional theory for rod-coil polymers with different size segments," J. Chem. Phys. **135**, 054903 (2011).
[50]R. Roth, R. Evans, A. Lang, and G. Kahl, "Fundamental measure theory for hard-sphere mixtures revisited: The white bear version," J. Phys.: Condens. Matter **14**, 12063 (2002).
[51]D. P. Cao and J. Z. Wu, "Density functional theory for semiflexible and cyclic polyatomic fluids," J. Chem. Phys. **121**, 4210 (2004).
[52]M. S. Wertheim, "Thermodynamic perturbation theory of polymerization," J. Chem. Phys. **87**, 7323 (1987).
[53]H. Chen and E. Ruckenstein, "Micellar structures in nanoparticle- multiblock copolymer complexes," Langmuir **30**, 3723 (2014).
[54]S. B. Jabes, H. O. S. Yadav, S. K. Kumar, and C. Chakravarty, "Fluctuation-driven anisotropy in effective pair interactions between nanoparticles: Thiolated gold nanoparticles in ethane," J. Chem. Phys. **141**, 154904 (2014).
[55]Ł. Baran and S. Sokołowski, "A comparison of molecular dynamics results for two models of nanoparticles with fixed and mobile ligands in two-dimensions," Appl. Surf. Sci. **396**, 1343 (2017).
[56]S. Plimpton, "Fast parallel algorithms for short-range molecular-dynamics," J. Comput. Phys. **117**, 1 (1995).
[57]For the description of the package see http://lammps.sandia.gov.
[58]W. R. Smith and I. Nezbeda, "The reference average Mayer-function (RAM) perturbation theory for molecular fluids," Adv. Chem. **204**, 235 (1983).
[59]A. A. Louis, "Effective potentials for polymers and colloids: Beyond the van der Waals picture of fluids?," Philos. Trans. R. Soc., A **359**, 939 (2001).
[60]J. A. Barker and D. Henderson, "What is 'liquid'? Understanding the states of matter," Rev. Mod. Phys. **48**, 587 (1976).
[61]M. Borówko, W. Rżysko, S. Sokołowski, and T. Staszewski, "Density functional approach to adsorption and retention of spherical molecules on surfaces modified with end-grafted polymers," J. Phys. Chem. B **113**, 4763 (2009).
[62]A. A. Louis, P. G. Bolhuis, and J. P. Hansen, "Mean-field fluid behavior of the Gaussian core model," Phys. Rev. E **62**, 7961 (2000).
[63]C. N. Likos, N. Hoffmann, H. Löwen, and A. A. Louis, "Exotic fluids and crystals of soft polymeric colloids," J. Phys.: Condens. Matter **14**, 7681 (2002).

[64]K. Xu, P. Zhu, C. Huh, and M. T. Balhoff, "Microfluidic investigation of nanoparticles' role in mobilizing trapped oil droplets in porous media," Langmuir **31**, 13673 (2015).

[65]T. Zhang, M. J. Murphy, H. Yu, H. G. Bagaria, K. Y. Yoon, B. M. Nielson, C. W. Bielawski, K. P. Johnston, C. Huh, and S. L. Bryant, *Investigation of Nanoparticle Adsorption During Transport in Porous Media* (Society of Petroleum Engineers, 2015), SPE-166346-PA.

[66]S. Li and O. Torsaeter, *The Impact of Nanoparticles Adsorption and Transport on Wettability Alteration of Intermediate Wet Berea Sandstone* (Society of Petroleum Engineers, 2015), SPE-172943-MS.

[67]S. Li, A. T. Kaasa, L. Hendraningrat, and O. Torsæter, "Effect of silica nanoparticles adsorption on the wettability index of Berea sandstone," in Paper SCA2013–059 presented at the International Symposium of the Society of Core Analysts held in Napa Valley, California, USA, 16–19 September 2013.